Ab initio study of longitudinal and transverse dynamics, including fast sound, in molten UO_2 and liquid Li-Pb alloys.

Beatriz G. del Rio[1] and Luis E. González[1]

Departamento de Física Teórica, Universidad de Valladolid, Valladolid,

SPAIN

(*Electronic mail: luisenrique.gonzalez@uva.es)

The disparity between the masses of the two components in a binary liquid system can lead to the appearance of a peculiar phenomenon named "fast sound", which was identified for the first time in Li_4Pb several decades ago, and later observed in other Li based alloys. However, the exact characteristics and nature of this phenomenon and the reasons behind its appearance have not totally been identified yet. In this work we analyze the longitudinal and transverse current correlation functions of UO_2, Li_4Pb, and $Li_{0.17}Pb_{0.83}$, as obtained from ab initio molecular dynamics simulations. We find that fast sound appears to occur in the two former systems but not in the latter. Additionally we discuss some of the properties of the liquid mixtures that may be related to the appearance (or absence) of the phenomenon, such as the composition, the polyhedral structure of the melt, and the type of bonding in the system.

I. INTRODUCTION

The understanding of the dynamic properties of liquids has been steadily increasing during the last decades thanks to experimental achievements that have improved the accuracy in the measurements, and also to molecular dynamics simulation techniques, which have adapted to the ever evolving computing power available, making them more and more realistic in the description of interatomic interactions. In particular, first principles molecular dynamics (FPMD) based on density functional theory (DFT)[1] represents nowadays one of the most accurate simulation methods available. Additionally, theoretical approaches have also played a substantial role in the field of atomic dynamics of liquids,[2–7] allowing the analysis and interpretation of experiments and simulations in terms of models and/or theories applicable in the different dynamic regimes characterized by different ranges of wavelengths and times probed.

In the long wavelength and long time regime the liquid behaves as a quasicontinuum and hydrodynamic theory is applicable. This leads to linearly dispersing and quadratically attenuating propagating longitudinal modes, corresponding to sound waves, and relaxing non-propagating modes, related to thermal diffusion and, in the case of binary systems, interdiffusion. Transverse excitations on the other hand decay only through viscous relaxation.

As the wavelength decreases the atomic nature of the liquid becomes relevant and other non-hydrodynamic (also called kinetic) modes become apparent (structural relaxation, viscoelasticity, possible heat waves, transverse waves, optical waves in binary systems, etc.) and interact with the hydrodynamic ones. This leads, among other effects, to a variation of the initially linear dispersion of the sound modes. In particular, the interaction of sound with structural relaxation leads to the so called positive sound dispersion, i.e., an increase in the phase velocity of the sound waves from the adiabatic speed of sound, c_s, towards the so called elastic, or high frequency, sound velocity, c_∞. This viscoelastic effect, that can be modulated by the interaction with thermal modes (either reinforcing it or counteracting it), is well understood,[8] and is ubiquitous in all liquid systems, either single-component (like Ar),[8] or molecular (like water)[9] or binary (like Na-K).[10]

There are however some specific features in the dynamics of binary liquids that are not so well understood and deserve further study. For instance, a longitudinal propagating mode of high energy has been recently detected in FPMD simulations of a molten salt,[11] whose frequency coincides with that of a transverse propagating mode. At present no theoretical scheme can explain such a "transverse-like" longitudinal mode.

2

Another feature, specific of binary systems with a large mass disparity between their components, is the appearance, in some cases, of the so called fast sound phenomenon, which was discovered in MD simulations of Li_4Pb,[12] and later observed in neutron scattering experiments of Li_4Pb and Li_4Tl.[13] The term refers to the existence of high frequency propagating excitations, observable in the dynamics of the light component, with a roughly constant phase velocity, similar to that of a liquid made up exclusively by the light component in the same thermodynamic state, which is much higher than the hydrodynamic speed of sound of the alloy. The name fast *sound* comes from the interpretation that assigns an acoustic character to these propagating excitations, but this interpretation has been challenged in other studies[14–16] where an optical character is proposed for these excitations, at least in the case of Li based alloys.

Such a fast propagating longitudinal mode has also been found in theoretical studies of low density mixtures of gases with disparate masses according to the revised Enskog theory.[17] This fast mode could in principle be observed experimentally as an extended shoulder in light scattering experiments if both gases have a similar polarizability.[18]

However, apart from a large mass ratio between components, there is at present no clear understanding of the particular properties of a multi-component system that are responsible for the appearance of fast sound. For instance, it is not known if Li-Pb alloys at other concentrations different from Li_4Pb, which obviously share the same mass ratio, display also fast sound.

It is somewhat remarkable that most of the high density liquid alloys where fast sound has been observed, either experimentally, like Li_4Pb and Li_4Tl,[13] or in simulations, like $Li_{0.7}Bi_{0.3}$,[19] are in fact Li based alloys. Obviously, the fact that Li has the smallest mass among metallic elements, and can be readily alloyed with heavy ones, is one of the reasons for the study of such systems. However, it is also interesting to note that all of these alloys show some degree of charge transfer from Li to the other component in the concentration region where fast sound was observed, as evinced by electrical resistivity measurements,[20,21] spin lattice relaxation studies,[22] or Knight shift experiments.[23] This fact may indicate that the type of bonding in the alloy (with partial charge transfer, but not fully ionic) could play some role in the appearance of fast sound.

Another interesting characteristic that has been recently observed in liquid Li_4Pb is the persistence of a polyhedral structure in the liquid,[24] somehow similar to that already present in the solid at nearby compositions.[25] Since the static structure directly affects the dynamic properties of liquids in the kinetic regime, it could also be argued whether such type of real-space atomic arrangement can have some influence on the appearance of fast sound.

In order to answer these questions, at least partially, we have reanalyzed previous FPMD simulations of Li_4Pb and $Li_{0.17}Pb_{0.83}$,[24] which share the mass ratio but differ in the composition and in the bonding type, the latter being a purely metallic alloy. Additionally we have performed FPMD simulations of molten UO_2 and analyzed the corresponding results for the dynamic properties. Molten oxides usually display a polyhedral networked structure[26] and some degree of ionicity in their bonding. The mass ratio between components in UO_2 is also quite large ($m_U/m_O \approx 15$ as compared to $m_{Pb}/m_{Li} \approx 30$). Note that UO_2 is a binary system (made up of U and O atoms) in which the heavy component, i.e. U, is minoritary, which is another point in common with Li_4Pb. According to the phase diagram,[27] at the temperature selected for the study (3200 K) the range of compositions where the liquid is the stable thermodynamic phase spans roughly from 55 to 70 atomic percent of O. We have selected the stoichiometric composition due to the existence of x-ray diffraction experiments at this composition[28] that can be used to assess the validity of the simulations performed. Therefore molten UO_2 is expected to share some of the characteristics of liquid Li_4Pb, possibly displaying also fast sound. Note that there has been no previous report of fast sound in molten oxides.

A final remark to mention is that both $Li_{0.17}Pb_{0.83}$, which corresponds to the Pb-rich lithium lead eutectic (LLE) composition, and UO_2 are important liquids in technological terms. The former is a candidate for its use as blanket in future tokamak fusion reactors such as DEMO, and the latter as it concerns the behaviour of the afterproducts of a core melt in case of loss of coolant type of accidents in nuclear fission reactors. Apart from their basic properties, their behaviour is most interesting when there are other elements dissolved in them, like tritium and helium in the case of the liquid LLE alloy, and Zr and other elements from the zircalloy cladding of the fuel, or atoms from the structural elements of the reactor, in the case of UO_2.

Studies of such systems with additional atomic species, especially at dilute concentrations, through FPMD is likely unfeasible beacause of the computational demands of this type of simulations. Therefore the construction of effective potentials looks in principle unavoidable. In this context the present results will be useful as benchmarks against which the validity of those effective potentials should be compared.

TABLE I. Input data for the systems studied in this work. ρ is the total ionic number density and T is the temperature. N denotes the number of particles in the simulation sample, L is the side of the cubic simulation box, and N_c is the number of equilibrium configurations, with Δt denoting the time-step.

	LLE [24]	Li$_4$Pb [24]	UO$_2$
N	247	330	186
ρ (Å^{-3})	0.0325	0.0436	0.0593
T (K)	775	1075	3200
L (Å)	19.661	19.634	14.639
code	PARSEC	PARSEC	VASP
N_c	28000	21000	20000
Δt (fs)	4	4	4.5

II. COMPUTATIONAL METHOD

The FPMD simulations performed for Li-Pb alloys[24] were carried out using the PARSEC code,[29] that uses a real space representation of the single-particle orbitals and the electronic density, and norm-conserving pseudopotentials for the description of the interactions between ions and valence electrons. The simulations of molten UO$_2$ have been carried out using the planewave based VASP code.[30] The ion-electron interactions were described in this case using PAW potentials.[31]

The VASP code also provides the possibility to go beyond DFT in the study of some systems, by including additional terms that may be important in particular situations. One such type of approach is DFT+U (where a Hubbard-like term is added to the hamiltonian), which is often important in the study of crystalline oxides where electronic correlation and crystal-field symmetry play a very important role.

In fact solid UO$_2$ is one such system, where including the Hubbard term is essential to get a good description of the structure below 30 K. The strength of the Hubbard term is given by a parameter U, and the previous studies have suggested a value between 3 and 5 eV for the f-orbitals of uranium (with an optimum value around 4 eV), and 0 eV (i.e. no application of the Hubbard-like term) for the oxygen atom, in order to obtain the correct description of the properties of crystalline UO$_2$ (see [32] and references therein). In the molten state, however, no crystalline symmetry is present, and therefore including a Hubbard term may not be necessary.
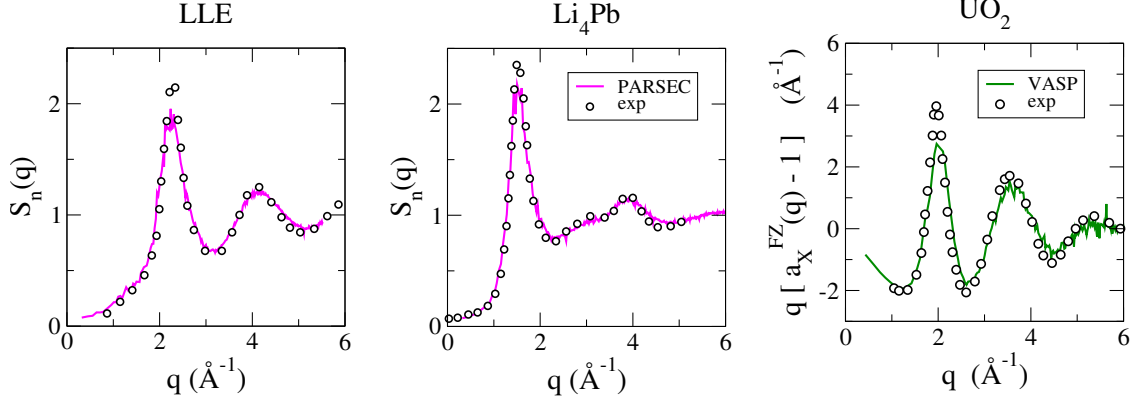
FIG. 1. Experimental and simulated total structure factors for liquid $Li_{0.17}Pb_{0.83}$ (left panel), Li_4Pb (central panel) and UO_2 (right panel). Symbols are experimental results (neutron diffraction in the case of Li-Pb alloys[33] and x-ray diffraction in the case of UO_2 [28]) and lines are FPMD results, with the Li-Pb ones taken from [24].
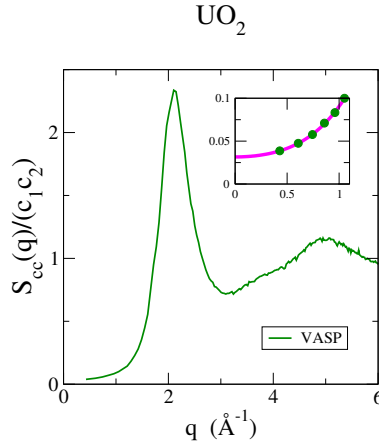

FIG. 2. Normalized Bhatia-Thornton concentration-concentration structure factor of molten UO_2. The inset shows the long wavelength behaviour together with a fit to a quadratic function.

In fact we have performed some calculations at the DFT+U level, with $U = 3.96$ eV, leading to results in poor agreement with some experimental data, such as the adiabatic speed of sound, which is highly overestimated. Consequently we consider below the results obtained from simulations at the DFT level, which appear as more reliable than the DFT+U case in the molten state.

Table I shows the details of the different FPMD simulations performed for the 3 systems that we are considering here. The simulation samples, which include a total of N particles, are enclosed

6

in a cubic box of side L consistent with the experimental density, which is periodically repeated. In the case of the UO_2 simulations we used the PAW potentials provided with the VASP distribution, which consider 6 and 14 valence electrons for O and U atoms respectively, and taken the cutoffs in the planewave expansions suggested by the developers of the potentials. After adequate thermalization, a number of N_c equilibrium configurations, separated by a time-step Δt, were generated and later used to analyze the properties of the sytems.

III. STRUCTURAL PROPERTIES

FPMD simulations are, as discussed above, highly precise, but nevertheless the accuracy should always be checked by comparing the obtained results against experimentally available data. In liquids the first magnitude to consider is the experimentally measured static structure factors, shown in figure 1. In the case of Li-Pb alloys, neutron scattering experiments were performed by Ruppersberg and coworkers[33] and it was already observed in [24] that the PARSEC simulations accounted very well for the measured total structure factor, $S_n(q)$, at all the concentrations considered. In the case of molten UO_2 the magnitude experimentally available is the Faber-Ziman total x-ray structure factor, $a_X(q)$.[28] We have computed this function from the FPMD generated configurations, observing a nice agreement with the experimental data. The main peak of the structure factor is located at $q_p = 2.35$, 1.60, and 1.98 Å^{-1} for the LLE, Li_4Pb and UO_2 systems respectively.

In the particular case of Li_4Pb, due to the values of the neutron scattering lengths of the isotopes, ^7Li and natural Pb, used in the experiments,[33] the total neutron weighted structure factor essentially coincides with the normalized Bhatia-Thornton concentration-concentration structure factor, $S_{cc}(q)/(c_1c_2)$, where c_i denotes the molar concentration of species i, and consequently the central panel of figure 1 is also showing this function. In fact this is an interesting magnitude, since in the long wavelegth limit it pictures the coordinating tendencies of the mixtures, with a value smaller than 1 indicating heterocoordinating tendencies. In figure 2 we show the FPMD results for $S_{cc}(q)/(c_1c_2)$ in UO_2. The inset highlights the low q behaviour and reveals that the system has a very strong compound forming tendency. Moreover, the results indicate that the bonding is not completely ionic, since in this case $S_{cc}(q)$ would vanish quadratically as $q \to 0$. The shape of $S_{cc}(q)/(c_1c_2)$ is in fact very similar to the one corresponding to Li_4Pb (see the central panel of figure 1) suggesting a similar type of chemical ordering. There are other magnitudes, in particular related to dynamic properties, that behave in a different way for ionic and non-ionic systems.[34]
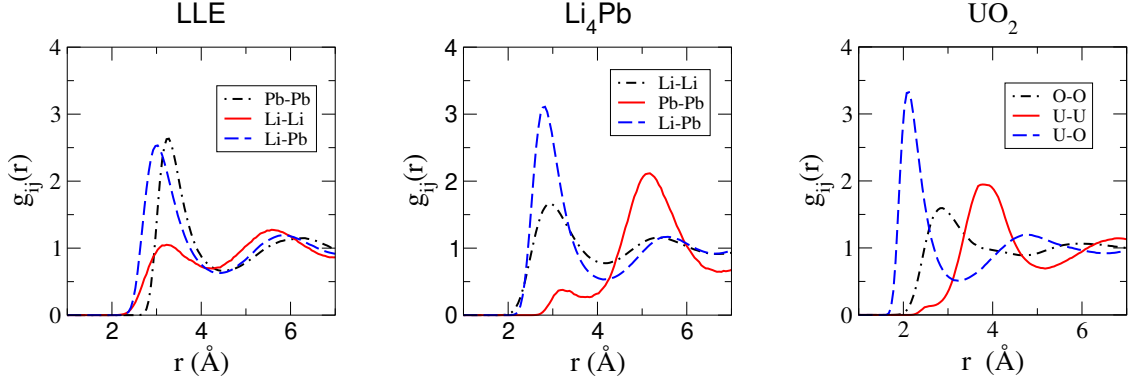
FIG. 3. Pair correlation functions, $g_{ij}(r)$, for liquid $Li_{0.17}Pb_{0.83}$ (left panel), Li_4Pb (central panel) and UO_2 (right panel). The continuous line corresponds to the like component of the minoritary species, dashed lines are the cross pair correlation functions, and dash-dotted lines denote the like component of the majoritary species.

These will be commented in the following sections, but we anticipate here that all of them indicate that the bonding is not fully ionic in UO_2.

The partial pair correlation functions $g_{ij}(r)$ are plotted in figure 3 for the three systems considered here. Looking at the correlation functions related to the minoritary component, we see in the three cases a small first peak followed by a higher second peak for the like component (i.e. $g_{LiLi}(r)$ in the LLE alloy, $g_{PbPb}(r)$ in Li_4Pb, and $g_{UU}(r)$ in UO_2), but the similarity between the functions for Li_4Pb and UO_2 is certainly striking. The cross terms have also a similar shape, while the like pair correlation function for the majoritary component is the one where more differences are observed.

Computing the average number of neighbours in the first spherical coordination shell around a minoritary component atom we obtain $n_{LiLi} = 0.8$ and $n_{LiPb} = 9.2$ in the LLE alloy, $n_{PbPb} = 0.3$ and $n_{PbLi} = 10.9$ in Li_4Pb, and $n_{UU} = 0.3$ and $n_{UO} = 5.9$ in UO_2.

Taking into account the very small values of the like minoritary component number of neighbours, the fact that some crystalline solids can be described in terms of interconnected polyhedra, and that the structure of liquid Li_4Pb can also be described in the same terms,[24] we have proceeded to analyse whether the structure of UO_2 and the LLE alloy can also be described that way.

In order to do so, for each configuration of the simulations we have selected an atom of the minority type, found the nearest unlike neighbours, i.e. those at a distance shorter than the position of the minimum of $r^2 g_{12}(r)$, and constructed the convex hull of that set of atoms. Then we have
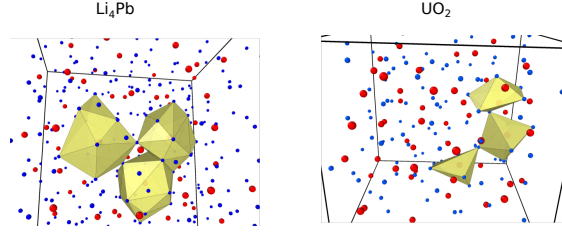
8

FIG. 4. Snapshots showing some polyhedra in Li_4Pb (left) and UO_2 (right). Red balls are Pb and U atoms, blue balls represent Li and O atoms. The pictures have been obtained using the Open VIsualization Tool (ovito) [36].

checked if any of the other atoms of the minority type are found within this convex hull. If none can be found, this means that the original selected atom has a polyhedron of unlike neighbours surrounding it. The procedure is then repeated for each atom of the minority type. If none of them has like atoms within the convex hull of the unlike neighbors, then the structure can indeed be described as an interconnecting polyhedral arrangement. The check is then repeated for all the configurations generated by the simulations.

The magnitude that tests the location of a point with respect to a convex polyhedron is the distance between them, which is positive/negative if the point is outside/inside the polyhedron. We have followed a simplified version of the Gilbert-Johnson-Keerthi algorithm[35] to obtain just the sign of the distance.

In the case of UO_2 we have found that the polyhedral structure applies perfectly. The most abundant polyhedra, around 40 % of the total, are formed by 6 oxygen atoms (UO_6 polyhedra, mostly distorted octahedra) although there are also UO_5 and UO_7 polyhedra with abundances around 20-25 % each, and smaller and larger polyhedra with minor abundances. We also remind that in Li_4Pb the most abundant polyhedra were $PbLi_{11}$, with other polyhedra also present ranging from $PbLi_7$ to $PbLi_{15}$ [24]. The tests for the liquid LLE alloy revealed that in 700 configurations (out of 28000 considered) there were Li atoms within the convex hull of the Pb neighbours of a different Li atom. This amounts roughly to a 2.5 % of the configurations, which is significantly different from zero. Therefore we cannot consider the structure as a polyhedral one, and note that this is also consistent with the fact that n_{LiLi} was near 1, meaning that on average one Li atom is a near neighbour of a different Li atom.

In figure 4 we show a snapshot of the simulation for Li_4Pb and UO_2 where three polyhedra are

9

displayed.

IV. COLLECTIVE DYNAMICS

We have investigated the spectra of the longitudinal and transverse current correlation functions, which for an isotropic system depend on the wavevector module $q \equiv |\vec{q}|$ and the frequency ω.

Whereas in a one-component system only one microscopic current (and density) can be defined in terms of the velocities and positions of the particles, in the case of binary systems several different sets of two microscopic currents (and densities) can be defined, and correspondingly three types of current correlation functions (and density correlation functions). The Ashcroft-Langreth (A-L) or component-wise set, and the Bhatia-Thornton (B-T) or number-concentration set, are quite standard in the study of binary liquids.[37] Additionally, the mass-composition (M-X)[38,39] set has also been considered. We will use a somewhat different normalization of the functions that highlights the matrix form of the magnitudes, so for completeness we describe them in detail in the next subsection. Then we report results for the spectra of the longitudinal and transverse correlation functions corresponding to the mass-composition set as compared with those of the component-wise set, and consider their dispersion relations.

A. Definitions

Consider a binary system of N atoms composed of N_1 atoms of mass m_1 and N_2 atoms of mass $m_2 > m_1$, with $N = N_1 + N_2$. The (molar) concentrations are $c_1 = N_1/N$ and $c_2 = N_2/N$, with $c_1 + c_2 = 1$. We define the average mass $\overline{m} = c_1 m_1 + c_2 m_2$, and the mass concentrations (which from now on will be called compositions) $x_1 = c_1 m_1/\overline{m}$ and $x_2 = c_2 m_2/\overline{m}$, with $x_1 + x_2 = 1$. We finally define two additional magnitudes $\delta_m = (m_1 - m_2)/\overline{m}$, and $y = c_1 c_2/(x_1 x_2) = \overline{m}^2/(m_1 m_2)$.

The component-wise, or A-L, or partial currents are

$$\begin{cases} \vec{j}_1(\vec{q},t) = \frac{1}{\sqrt{N_1}} \sum_{l_1=1}^{N_1} \vec{v}_{l_1}(t) \exp[-i\vec{q} \cdot \vec{r}_{l_1}(t)] \\ \\ \vec{j}_2(\vec{q},t) = \frac{1}{\sqrt{N_2}} \sum_{l_2=1}^{N_2} \vec{v}_{l_2}(t) \exp[-i\vec{q} \cdot \vec{r}_{l_2}(t)], \end{cases} \qquad (1)$$

10

where $\vec{r}_l$ and $\vec{v}_l$ denote the position and velocity of particle l, and the indexes l_1 and l_2 run over particles of type 1 and 2 respectively.

From these two functions one can define the number-concentration, or B-T normalized currents as

$$
\begin{pmatrix} \vec{j}_N \\ \dfrac{\vec{j}_c}{\sqrt{c_1 c_2}} \end{pmatrix} = \begin{pmatrix} \sqrt{c_1} & \sqrt{c_2} \\ \sqrt{c_2} & -\sqrt{c_1} \end{pmatrix} \begin{pmatrix} \vec{j}_1 \\ \vec{j}_2 \end{pmatrix}.
\tag{2}
$$

Explicitly, we have

$$
\vec{j}_N(\vec{q},t) = \frac{1}{\sqrt{N}} \sum_{l=1}^{N} \vec{v}_l(t) \exp[-i\vec{q} \cdot \vec{r}_l(t)]
\tag{3}
$$

where l now runs over all of the particles of the system. Likewise, in the limit $\vec{q} = 0$ the normalized concentration current reduces to

$$
\frac{\vec{j}_c(0,t)}{\sqrt{c_1 c_2}} = \sqrt{\frac{N_1 N_2}{N}} \left(\frac{1}{N_1} \sum_{l_1=1}^{N_1} \vec{v}_{l_1}(t) - \frac{1}{N_2} \sum_{l_2=1}^{N_2} \vec{v}_{l_2}(t) \right)
\tag{4}
$$

and is therefore proportional to the relative velocity of the centers of mass of particles of different type. Consequently, the normalized concentration current is related to interdiffusion processes in the hydrodynamic regime, and also to waves of optical character at other values of q.

The third set of currents is the M-X set. It is defined by

$$
\begin{pmatrix} \vec{j}_m \\ \dfrac{\vec{j}_x}{\sqrt{x_1 x_2}} \end{pmatrix} = \mathscr{X} \mathscr{M} \begin{pmatrix} \vec{j}_1 \\ \vec{j}_2 \end{pmatrix},
\tag{5}
$$

where the matrices $\mathscr{X}$ and $\mathscr{M}$ are

$$
\mathscr{X} = \begin{pmatrix} \sqrt{x_1} & \sqrt{x_2} \\ \sqrt{x_2} & -\sqrt{x_1} \end{pmatrix}, \quad \mathscr{M} = \begin{pmatrix} \sqrt{\frac{m_1}{m}} & 0 \\ 0 & \sqrt{\frac{m_2}{m}} \end{pmatrix}.
\tag{6}
$$

Obviously, this set can also be obtained from the B-T one, the relation being

$$
\begin{pmatrix} \vec{j}_m \\ \dfrac{\vec{j}_x}{\sqrt{x_1 x_2}} \end{pmatrix} = \begin{pmatrix} 1 & \delta_m \sqrt{c_1 c_2} \\ 0 & 1/\sqrt{y} \end{pmatrix} \begin{pmatrix} \vec{j}_N \\ \dfrac{\vec{j}_c}{\sqrt{c_1 c_2}} \end{pmatrix},
\tag{7}
$$

where it is observed that the composition current is proportional to the concentration current and therefore both represent the same dynamic property.

11

All the microscopic currents just defined can be decomposed into their longitudinal and transverse components, parallel and perpendicular to the wavevector $\vec{q}$ respectively.

$$j_\alpha^L(\vec{q},t) = \vec{u}_q \cdot \vec{j}_\alpha(\vec{q},t) \tag{8}$$

$$\vec{j}_\alpha^T(\vec{q},t) = \vec{j}_\alpha(\vec{q},t) - j_\alpha^L(\vec{q},t)\,\vec{u}_q\,, \tag{9}$$

where $\vec{u}_q = \vec{q}/q$, is a unit vector along $\vec{q}$, and α can be any of $\{1,2,N,c,m,x\}$.

From these sets of collective microscopic functions, the matrices of longitudinal and transverse current correlation functions are defined as

$$\mathscr{C}^L(q,t) = \begin{pmatrix} C_{\alpha\alpha}^L(q,t) & C_{\alpha\beta}^L(q,t) \\ C_{\beta\alpha}^L(q,t) & C_{\beta\beta}^L(q,t) \end{pmatrix} =$$

$$\left\langle \begin{pmatrix} j_\alpha^L(\vec{q},t) \\ j_\beta^L(\vec{q},t) \end{pmatrix} \begin{pmatrix} j_\alpha^{L*}(\vec{q},0) & j_\beta^{L*}(\vec{q},0) \end{pmatrix} \right\rangle, \tag{10}$$

with the asterisk denoting complex conjugation, and

$$\mathscr{C}^T(q,t) = \begin{pmatrix} C_{\alpha\alpha}^T(q,t) & C_{\alpha\beta}^T(q,t) \\ C_{\beta\alpha}^T(q,t) & C_{\beta\beta}^T(q,t) \end{pmatrix} =$$

$$\frac{1}{2} \left\langle \begin{pmatrix} \vec{j}_\alpha^T(\vec{q},t) \\ \vec{j}_\beta^T(\vec{q},t) \end{pmatrix} \cdot \begin{pmatrix} \vec{j}_\alpha^{T*}(\vec{q},0) & \vec{j}_\beta^{T*}(\vec{q},0) \end{pmatrix} \right\rangle. \tag{11}$$

In the previous equations, the averages are taken over time origins and over wavevectors with the same module. Their Fourier Transforms into the frequency domain are the corresponding matrices of longitudinal and transverse current spectra, $\mathscr{C}^L(q,\omega)$ and $\mathscr{C}^T(q,\omega)$.

Note that in fact all the matrices are symmetric, i.e. $C_{\alpha\beta} = C_{\beta\alpha}$. In the case of the A-L set the correlation functions are then C_{11}, C_{12} and C_{22}. In the case of the B-T set they are $C_{NN}, C_{Nc}/\sqrt{c_1 c_2}$ and $C_{cc}/(c_1 c_2)$. And in the case of the M-X set they are $C_{mm}, C_{mx}/\sqrt{x_1 x_2}$ and $C_{xx}/(x_1 x_2)$.

Any correlation function from a given set is a linear combination of the three correlation functions of any other set. For instance,

$$C_{mm} = \alpha_{mm}^{11} C_{11} + \alpha_{mm}^{12} C_{12} + \alpha_{mm}^{22} C_{22}\,,$$

TABLE II. Mass and concentration parameters and coefficients relating the A-L functions to the M-X ones and viceversa.

	LLE	Li$_4$Pb	UO$_2$
c_1	0.17	0.80	2/3
c_2	0.83	0.20	1/3
m_1 (u)	6.94	6.94	16.000
m_2 (u)	207.2	207.2	238.029
$\overline{m}$ (u)	173.156	46.992	90.0097
x_1	0.0068	0.118148	0.118506
x_2	0.9932	0.881852	0.881494
α_{mm}^{11}	0.000273082	0.0174486	0.0210654
α_{mm}^{12}	0.0360304	0.520944	0.443195
α_{mm}^{22}	1.18846	3.88832	2.3311
α_{mx}^{11}	0.00329703	0.0476701	0.0574527
α_{mx}^{12}	0.216012	0.616277	0.523123
α_{mx}^{22}	-0.098436	-1.42323	-0.854713
α_{xx}^{11}	0.0398064	0.130236	0.156693
α_{xx}^{12}	-0.0360304	-0.520944	-0.443195
α_{xx}^{22}	0.00815312	0.520944	0.313387
α_{11}^{mm}	0.17	0.8	0.666667
α_{11}^{mx}	4.10496	4.37124	3.63646
α_{11}^{xx}	24.7804	5.97118	4.95894
α_{12}^{mm}	0.375633	0.4	0.471405
α_{12}^{mx}	4.50405	0.9464	1.11284
α_{12}^{xx}	-0.375633	-0.4	-0.471405
α_{22}^{mm}	0.83	0.2	0.333333
α_{22}^{mx}	-0.137492	-0.146411	-0.244438

and similar expressions for the functions $C_{mx}/\sqrt{x_1 x_2}$ and $C_{xx}/(x_1 x_2)$. Also, we have

$$C_{11} = \alpha_{11}^{mm} C_{mm} + \alpha_{11}^{mx} \frac{C_{mx}}{\sqrt{x_1 x_2}} + \alpha_{11}^{xx} \frac{C_{xx}}{x_1 x_2},$$

and similar expressions for C_{12} and C_{22}. The $\alpha_{k\ell}^{ij}$ coefficients are easily obtained in terms of the elements of matrices $\mathscr{X}$ and $\mathscr{M}$. In table II we list the values of the concentrations, masses, average mass, compositions and coefficients to obtain the M-X functions from the A-L ones and viceversa, for the three systems considered. In the three cases the heavy component has the largest composition ($x_2 > x_1$), even when it is minoritary in terms of molar concentrations ($c_2 < c_1$). Curiously the compositions for $Li_4 Pb$ and UO_2 are practically identical. Note that C_{mm} is dominated by the heavy partial, C_{22}, with a coefficient α_{mm}^{22} at least 100 times larger than the one corresponding to light component, α_{mm}^{11}, and 5 times larger than the coefficient of the cross term, α_{mm}^{12}.

Clearly, all the sets convey the same information. However, their behaviour can be different in different dynamic regimes, and shed some light about which are the fundamental physical mechanisms that rule the dynamic properties of the system in those regimes.

For instance, in the limit of large q, which samples small real-space regions, particles will not practically feel the presence of the other ones, and therefore the dynamic properties will be determined by the single-particle behaviour, and in particular a component-wise description will be optimal. In the other limit, where q is small and consequently large real-space regions are sampled, the hydrodynamic theory is applicable, which deals basically with the balance of mass, momentum and energy, and therefore the M-X set is the most adequate to describe the dynamics of the system. In fact the behaviour of the M-X correlation functions in this regime (except for very short times) must obey the predictions of the hydrodynamic theory. Finally if one is interested in the dynamics of topological magnitudes, valuable information is obtained from the B-T set, where the N current considers all the atoms at the same level without taking into account their chemical species.

Note that the partial (A-L) densities ρ_1 and ρ_2 are obtained by dropping the velocities in the respective sums of equation 1. The corresponding B-T (ρ_N and $\rho_c/\sqrt{c_1 c_2}$) and M-X (ρ_m and $\rho_x/\sqrt{x_1 x_2}$) densities are defined through the same matrices of equations 2 and 5, respectively. The density correlation functions (partial intermediate scattering functions) are then obtained in a similar way as in equation 10, and their Fourier Transform into the frequency domain define the corresponding partial dynamic structure factors.

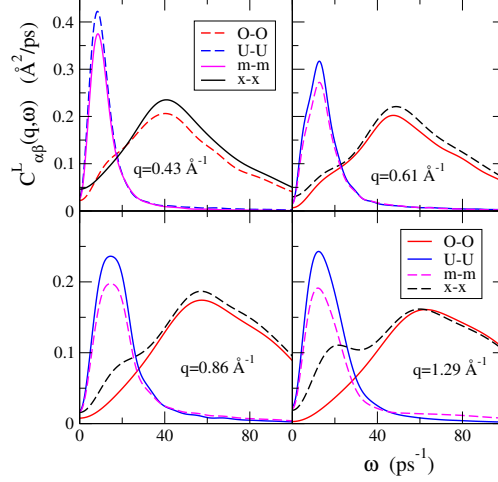The behaviour of the M-X and B-T density correlation functions and dynamic structure factors

FIG. 5. Longitudinal current correlation spectra for UO_2 at several wavevectors. Red line: $\alpha_{xx}^{OO} C_{OO}^L(q, \omega)$. Blue line: $C_{UU}^L(q, \omega)$. Magenta line: $\alpha_{UU}^{mm} C_{mm}^L(q, \omega)$. Black line: $C_{xx}^L(q, \omega)/(x_1 x_2)$. Continuous lines: single-mode functions. Dashed lines: double-mode functions.

in binary mixtures in the hydrodynamic limit was considered by Cohen, Sutherland and Deutch[38] and Bhatia, Thornton and March.[39] The set of variables that define hydrodynamics (the hydrodynamic variables) are the mass density ρ_m, the composition density ρ_x, the mass current $\vec{j}_m$ and the energy density. As a consequence of the linearized hydrodynamics equations, three hydrodynamic modes appear in the M-X density correlation functions, and consequently in the corresponding longitudinal currents, namely, two relaxing modes associated to thermal diffusion and interdiffusion, and a sound propagation mode, which appears in the *mm* correlation functions but not in the *xx* ones. Decoupled from these, a viscous shear relaxation mode appears in the transverse *mm* current correlation function.

In actual calculations of the correlation functions in MD simulations, additional non-hydrodynamic modes are routinely present, such as structural relaxation modes, shear waves, or optic like longitudinal and transverse modes. Sometimes such modes appear only for q larger than a critical value, but other modes can still be present for $q \to 0$. In this case their amplitude must vanish at least quadratically for small q, and the corresponding damping rates take a non-zero value in this limit. In the particular case of ionic systems charge neutrality imposes important constraints that modify some of these rules. In particular, optical modes show a non-zero weight at small wavevectors and contribute to the *xx* density correlation functions with an oscillating term which is absent in non-ionic systems.[34] In fact we have found no indication of such a term in any of the

15

three systems studied, pointing again to a non-ionic character of UO_2 in particular.

B.   Longitudinal and transverse currents

We discuss below separately the longitudinal and transverse current correlation spectra for the three systems studied.

1. UO_2

We plot in figure 5 the FPMD longitudinal current spectra of UO_2 at several wavevectors. The $C_{11}^L(q, \omega)$ functions ($1 \equiv O$) have been scaled by α_{xx}^{11} and the $C_{mm}^L(q, \omega)$ by α_{22}^{mm} (see table II) so as to plot all the functions in the same scale. For $q = q_{min} = 0.43$ Å^{-1} we observe that the M-X functions have a single peak, whereas the A-L functions (in particular C_{OO}^L) display a two-mode structure with a peak at the same position as that of C_{xx}^L and a shoulder near the position of the peak of C_{mm}^L. We can therefore conclude that for such a wavevector the dynamics is determined by the M-X variables, while the partial functions come as a combination of the latter.

Note that even if the dynamics is determined by the hydrodynamic variables this does not mean that this wavevector is in the hydrodynamic regime, since the high-frequency peak of C_{xx}^L shows up very clearly and corresponds to an optical mode, which as commented above vanishes quadratically with q in the hydrodynamic regime.

The situation is exactly opposite for the two largest wavevectors shown in figure 5, where it is now the A-L set that shows a single peak while the M-X set (in particular C_{xx}^L) shows a double-mode structure with a peak at the same position as that of C_{OO}^L and a shoulder or another peak at the position of C_{UU}^L.

This means that as q increases the dynamics of the system evolves from being driven by the M-X variables to being determined by the partial (A-L) variables. The situation at $q = 0.61$ Å^{-1} is intermediate, so that this wavevector stands at the transition region between the two types of dynamics.

These results generalize those obtained by Bryk and coworkers[14,15] when they analyzed results of classical molecular dynamics simulations for the dynamic structure factors of Li_4Pb and Li_4Tl, using the generalized collective modes (GCM) approach. They found that the frequencies of the modes obtained with a large set of dynamic variables could be reproduced in the low q region by
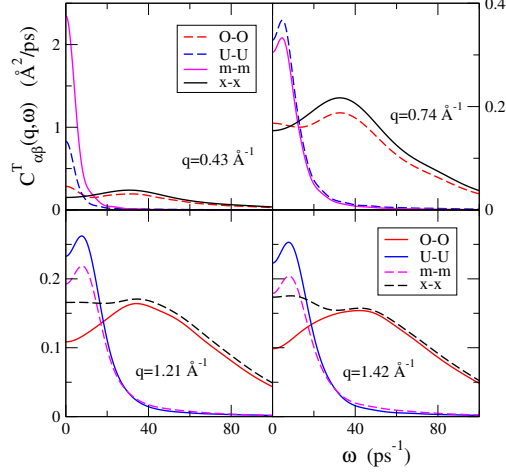
FIG. 6. Transverse current correlation spectra for UO$_2$ at several wavevectors. Red line: $\alpha_{xx}^{OO} C_{OO}^{T}(q, \omega)$. Blue line: $C_{UU}^{T}(q, \omega)$. Magenta line: $\alpha_{UU}^{mm} C_{mm}^{T}(q, \omega)$. Black line: $C_{xx}^{T}(q, \omega)/(x_1 x_2)$. Continuous lines: single-mode functions. Dashed lines: double-mode functions.

a GCM analysis involving only the hydrodynamic variables, while for larger q the mode frequencies were well reproduced by the GCM results obtained by considering only the partial dynamic variables, so that a transition from M-X driven to partial dynamics applies as q increases. Our data shows that the transition is not only observed in the mode frequencies, but in the whole shape of the correlation functions.

Figure 6 displays the transverse current correlation spectra for several values of q (note that they are not the same as those in figure 5). The qualitative behaviour is similar to that of the longitudinal current spectra with a crossover from M-X driven dynamics at small q values (the A-L partials, in particular the O-O partial, show a double mode structure) to A-L dictated dynamics at larger q, where the M-X functions, in particular, the C_{xx}^{T}, display a two-mode shape. There is a quantitative difference concerning the wavevector region where this transition takes place. In the case of the transverse dynamics this occurs for higher q values than for the longitudinal dynamics, being located around $0.9 - 1.0$ Å^{-1} as compared to $0.5 - 0.6$ Å^{-1} in the longitudinal case.

Additionally the propagation gap for shear waves can also be observed in figure 6, as C_{mm}^{T} does not show a finite frequency maximum at the lowest wavevector $q = q_{min}$, whereas it does for higher q.
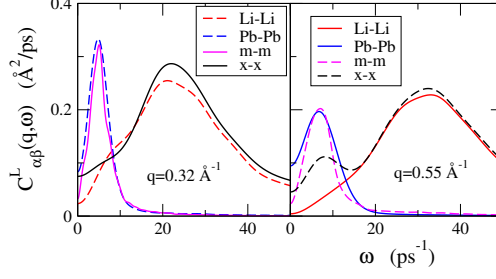
17

FIG. 7. Longitudinal current correlation spectra for Li_4Pb at several wavevectors. Red line: $\alpha_{xx}^{LiLi}C_{LiLi}^{L}(q,\omega)$. Blue line: $C_{PbPb}^{L}(q,\omega)$. Magenta line: $\alpha_{PbPb}^{mm}C_{mm}^{L}(q,\omega)$. Black line: $C_{xx}^{L}(q,\omega)/(x_1x_2)$. Continuous lines: single-mode functions. Dashed lines: double-mode functions.
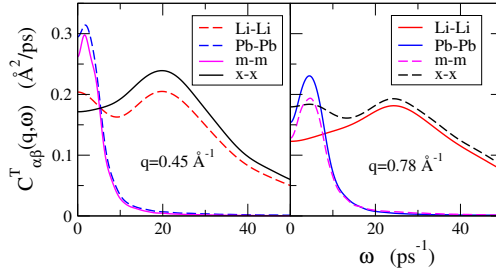

FIG. 8. Transverse current correlation spectra for Li_4Pb at several wavevectors. Magenta line: $\alpha_{PbPb}^{mm}C_{mm}^{T}(q,\omega)$. Black line: $C_{xx}^{T}(q,\omega)/(x_1x_2)$. Red line: $\alpha_{xx}^{LiLi}C_{LiLi}^{T}(q,\omega)$. Blue line: $C_{PbPb}^{T}(q,\omega)$. Continuous lines: single-mode functions. Dashed lines: double-mode functions.

2. Li_4Pb

The longitudinal and transverse current correlation spectra corresponding to liquid Li_4Pb are shown in figures 7 and 8 respectively. The general behaviour of both spectra is very similar to that of UO_2, i.e., for small q the dynamics of the system is dictated by the MX set, and after a transition region it turns to be component-wise dominated for higher wavevectors.

The main difference between Li_4Pb and UO_2 is quantitative, since the crossover region is now located at smaller wavevectors. In the longitudinal case the smallest q value (0.32 Å^{-1}) is already in the transition region, since $C_{xx}^{L}(q,\omega)$ shows a small shoulder at low frequencies. The lack of low frequency peaks or shoulders in $C_{LiLi}^{L}(q,\omega)$ at $q = 0.55$ Å^{-1} shows that this wavevector is already in the AL-dominated region. In the case of transverse currents the crossover region is located around $q = 0.6 - 0.7$ Å^{-1}, to be compared with the $0.9 - 1.0$ Å^{-1} range in the case of
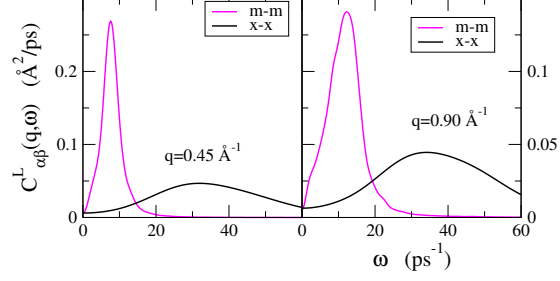
FIG. 9. Longitudinal current correlation spectra for the liquid LLE alloy at several wavevectors. Magenta line: $\alpha_{PbPb}^{mm}C_{mm}^{L}(q,\omega)$. Black line: $C_{xx}^{L}(q,\omega)/(x_1 x_2)$.
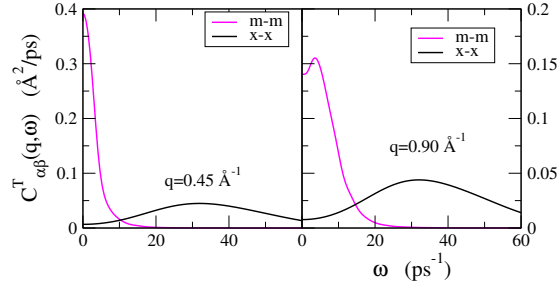

FIG. 10. Same as figure 9 but for transverse current correlation spectra.

UO_2. Note also that the crossover region for transverse currents occurs at higher wavevectors than the one corresponding to longitudinal dynamics, in the same way as it happened in UO_2.

The fact that the transition from MX to AL driven dynamics occurs at lower q-values in Li_4Pb than in UO_2 is directly related to the larger mass ratio in the former, which hinders low frequency oscillations of the light atoms due to the higher value of their natural frequencies as compared to those of the heavy ones.

3. $Li_{0.17}Pb_{0.83}$

The case of the liquid LLE, as compared to the other two systems considered here, is extremely simple, because as one observes in table II the mass-mass functions are basically equivalent to the Pb-Pb ones (α_{mm}^{22} overwhelmingly dominates over α_{mm}^{11} and α_{mm}^{12}), and the Li-Li functions are basically equivalent to the composition-composition ones (α_{11}^{xx} is also dominating). This means that MX and AL dynamics are basically one and the same. Note also that the composition of Pb in this system is very close to 1, so that from the mass-composition point of view the liquid LLE
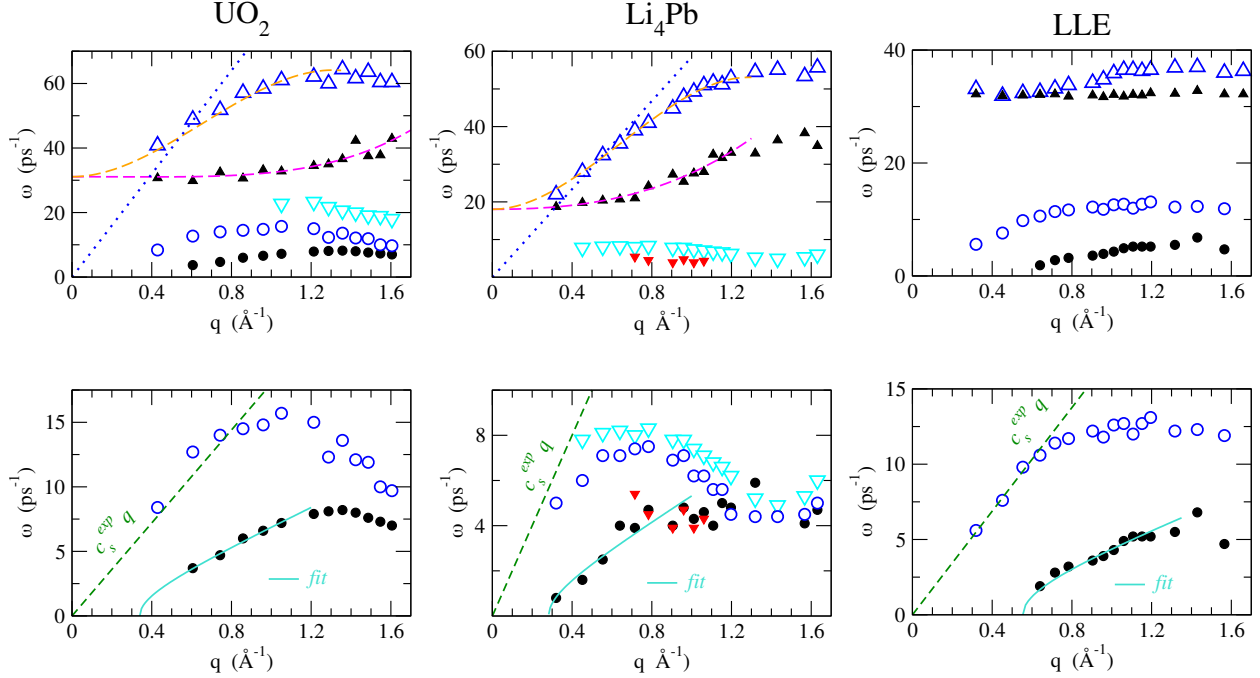
19

FIG. 11. Longitudinal (open symbols) and transverse (filled symbols) dispersion relations of the *mm* and *xx* currents for the three systems studied. Left panel: UO_2. Central panel: Li_4Pb. Right panel: LLE. Circles denote *mm* frequencies and triangles denote *xx* frequencies. Up triangles correspond to the high frequency peak of the *xx* spectra, $\omega_{xx}^{LO}(q)$ and $\omega_{xx}^{TO}(q)$, whereas down triangles correspond to the second, low frequency, peak of these functions, $\omega_{xx}^{L\ell}(q)$ and $\omega_{xx}^{T\ell}(q)$, when they exist (and are non-zero). Dashed lines in the upper figures are guides to the eye, that show a common extrapolation limit to $q=0$ for the longitudinal and transverse high frequency peaks. The dotted lines in the upper figures are plaussible extrapolations of the longitudinal high energy dispersion towards $q=0$ according to a (fast) sound-like behaviour. The bottom graphs display the low frequency region, so as to highlight the behaviour of the *mm* frequencies, $\omega_{mm}^{L}(q)$ and $\omega_{mm}^{T}(q)$ (note that in the case of Li_4Pb the *mm* frequencies have not been included in the upper graph in order not to overcrowd it). The dashed lines in these lower graphs represent the linear dispersion corresponding to hydrodynamic sound with the experimental adiabatic sound velocities. The solid line is a fit to equation 12 corresponding to a viscoelastic model for shear waves (see text).

is very dilute in Li.

Figures 9 and 10 show the longitudinal and transverse current correlation spectra for two values of q, where, as mentioned previously, we observe single peaks in the MX functions for any wavevector, and the only feature worth mentioning is the propagation gap at small q for transverse waves.

C. Dispersion relations

Figure 11 shows the dispersion relations associated to longitudinal and transverse mass-mass and composition-composition currents for the three systems studied. These graphs condense a lot of information about the collective dynamics of the systems, as we detail below.

The left panel shows the dispersion relations corresponding to UO_2. The upper graph shows the whole frequency range, while in the lower graph the frequency range covered corresponds to the excitations of the *mm* currents. The behaviour of these *mm* frequencies (ω^L_{mm} and ω^T_{mm}) is quite similar to the dispersion relations shown in one-component systems. The longitudinal excitations correspond to sound waves and their dispersion tends towards the hydrodynamic linear one ($\omega^L_{mm}(q) = c_s q$) as q goes to zero. The agreement with the experimental adiabatic sound velocity, $c_s^{exp} = 1800$ m/s,[40] is very good. For increasing q a typical positive dispersion is observed, followed by a maximum around half the position of the main peak in the structure factor, q_p, and a minimum around this wavevector. The transverse excitations correspond to shear waves. These only appear after a finite propagation gap, since liquids show a viscous, not elastic, behaviour at the scales sampled for small q. Near the edge of the propagation gap the frequencies of shear waves are well described by a viscoelastic model, with

$$\omega^T_{mm}(q) = \phi_T \sqrt{q^2 - q_c^2}. \tag{12}$$

This equation stems from the assumption of a Maxwell relaxation time in the transverse dynamics, that relates in the long wavelength limit the shear viscosity and the high frequency shear modulus of the liquid. Taking this to the equations that govern the transverse dynamics and imposing the existence of maxima in the transverse current spectrum leads to equation 12 (see, for instance, reference [4]). The parameters represent the minimum wavevector where shear waves appear, q_c, and the slope of the parabola, ϕ_T, for q somewhat larger than q_c. In the case of UO_2 the values of these parameters are $q_c = 0.340$ Å^{-1} and $\phi_T = 730$ m/s. Due to its derivation equation 12 ceases to be valid for increasing values of q as is readily seen in figure 11.

The behaviour of the *xx* dispersion relations is more interesting. First of all one can observe the existence of high frequency optic like excitations, both longitudinal (ω^{LO}_{xx}) and transverse (ω^{TO}_{xx}) in the whole q range. For small q these are the only peaks existing in C_{xx}, indicating as commented above that the dynamics of the system is ruled by the MX set. Moreover, in the limit $q \to 0$ the longitudinal and transverse optic frequencies can well be extrapolated to a common value,

21

$\omega_{xx}^{LO}(q \to 0) = \omega_{xx}^{TO}(q \to 0)$, as suggested by the dashed lines in the graph. This is the correct behavior for non-ionic mixtures, as is the case of UO_2 at the DFT level. On the contrary, if the system were ionic then there would be a gap between the longitudinal optic and transverse optic frequencies at $q = 0$.

For higher q the C_{xx} functions develop the second, low frequency peak, $\omega_{xx}^{L\ell}(q)$ and $\omega_{xx}^{T\ell}(q)$, that is located near the *mm* peak, whose ultimate origin is the dynamics of the heavy component, in this case U. The appearance of a second branch in the dispersion relation of the *xx* currents serves therefore to signal the transition to the wavevector region of component-wise dictated dynamics. Note that $\omega_{xx}^{T\ell}(q)$ can in some cases be located at $\omega = 0$ (see figure 6). Such values have not been represented in figure 11.

The central panel displays the dispersion relations corresponding to Li_4Pb. Almost everything said about UO_2 can be repeated for Li_4Pb. The sound dispersion does not show a clear positive dispersion, but is in good agreement with the experimental sound velocity of 2000 m/s.[41] The propagation gap for shear waves, as obtained by the fit to the viscoelastic model is $q_c = 0.283$ Å^{-1}, and the slope of the parabola is $\phi_T = 557$ m/s. The longitudinal and transverse optic frequencies can be extrapolated to a common value for $q \to 0$, and the second branches of low frequency excitations of the *xx* currents, driven by the dynamics of Pb atoms, appear at lower wavevectors than in UO_2, as we had already indicated above.

The right panel corresponds to the liquid LLE alloy. In this case the behaviour is very simple, with well separated *mm* and optical *xx* frequencies, no LO-TO gap, and no second branches for the *xx* excitations due to the practical identity between MX and AL dynamics in this system. The sound dispersion shows an excellent agreement with the experimental sound velocity of 1720 m/s,[42] displaying no positive dispersion, and shear waves start propagating at $q_c = 0.554$ Å^{-1}, with $\phi_T = 523$ m/s.

D. Fast sound?

Observation of the behaviour in the LLE alloy of the high frequency branch of the longitudinal and transverse dispersion relations (that correspond to the *xx* terms) gives direct evidence of its optical character. Even though oscillations with these frequencies appear in C_{11}^L, which is basically equivalent to C_{xx}^L for this system, it cannot be claimed that these excitations are sound waves of high frequency supported by the light component only, i.e., they do not qualify as fast sound.

Basically because these excitations are not dispersive, since the frequency does not change with q, at small wavevectors.

The situation for Li$_4$Pb is different. Even though the transverse high frequency branch is still non-dispersive for small q, this is not the case for the high frequency longitudinal branch. The latter can be extrapolated towards $q = 0$ so as to match the transverse branch, as shown by the dashed lines in figure 11, which is the correct behaviour in non-ionic systems. But if one focuses exclusively on ω_{xx}^L, without considering also the transverse counterpart, it looks also reasonable to extrapolate the data towards $q = 0$ using a straight line that goes through the origin, that is, using the behaviour of a sound wave of high velocity, as shown by the dotted line in the figure. And therefore call it fast sound. The key factor here is that the longitudinal xx branch is strongly dispersing, as opposed to its behaviour in the LLE alloy.

In the case of UO$_2$ the situation is similar to Li$_4$Pb. The longitudinal high frequency branch is also strongly dispersive, and compatible with a sound-like behaviour (see dotted line in the graph) if one assumes some degree of positive dispersion. And therefore UO$_2$ could also qualify as a system where fast sound can be observed. We rather consider instead that the extrapolation suggested by the dashed line in figure 11 has more physical sense, taking also into account the behaviour of the transverse high frequency branch.

It is interesting to note that the dispersive/non-dispersive character of the longitudinal xx high frequency branch is already present at the level of the frequency moments of the corresponding currents, as observed in figure 12. These are defined as

$$\omega_{xx}^{L\,(2)}(q) = \frac{\int_{-\infty}^{\infty} d\omega\, \omega^2 C_{xx}^L(q,\omega)}{\int_{-\infty}^{\infty} d\omega\, C_{xx}^L(q,\omega)} \tag{13}$$

and can be interpreted as "bare" elastic-like frequencies which get renormalized through the interactions with other modes, leading to the final dispersion relations. In the case of the Li$_4$Pb alloy, we observe that the renormalization in fact enhances the dispersive character of the xx branch, which is not the case for the LLE alloy or UO$_2$, where it amounts to a basically constant shift in the frequencies.

The question posed in the introduction about which factors enhance the possibility of observing fast sound in an alloy, could therefore be better reformulated as "which factors are mostly responsible for the existence of a strongly dispersing longitudinal xx high frequency branch in the dynamics of an alloy?" Obviously, by studying only three systems it is not possible to provide a definite answer, but we can signal some points.
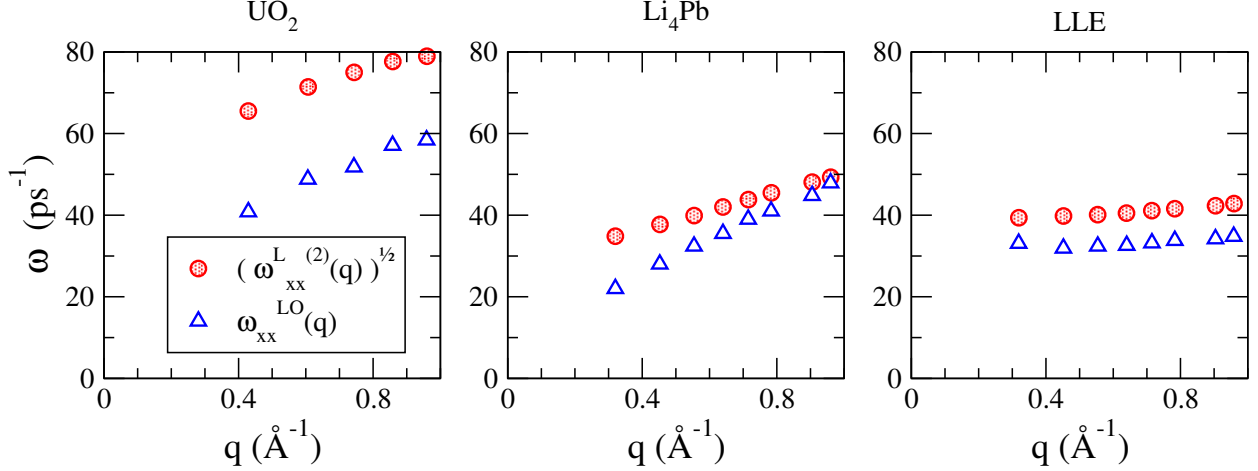
FIG. 12. Comparison between the second moments of $C_{xx}^{L}(q, \omega)$, $\omega_{xx}^{L\,(2)}(q)$, and the positions of the high frequency peaks, $\omega_{xx}^{LO}(q)$.

First, the large mass ratio between the components is a necessary condition, but clearly it is not sufficient, since the LLE alloy has the same mass ratio as Li_4Pb and their behaviour is totally opposite.

Second, the heavy element is minoritary in terms of molar concentration in both Li_4Pb and UO_2, and also in those other Li based alloys where fast sound was observed. Note however that in terms of composition (mass concentration) U and Pb are majoritary in UO_2 and Li_4Pb respectively, although not as overwhelmingly mass majoritary as Pb in the LLE.

Third, a common feature in liquid Li_4Pb and molten UO_2 not shared by the liquid LLE alloy is the polyhedral structure. Even though the polyhedra in the two systems are very different in the number of vertices, this type of structure could have some influence on the dynamics.

Fourth, both in liquid Li_4Pb and in molten UO_2 the bonding is dictated by some charge transfer, although not complete (i.e. not leading to an ionic bond). The strengths of the bonds are certainly different, as reflected by the large difference in the melting temperatures, but their character is similar. On the other hand the liquid LLE is a purely metallic system. As mentioned in the introduction other Li based alloys where fast sound has been observed also share this same partial charge transfer.

We therefore consider that it would be interesting to study if those other systems that display fast sound also show a polyhedral structure so as to clarify if this feature is really relevant. Other systems of interest would be Li-Pb alloys with $c_{Li} > 0.8$, where Pb continues to be minoritary, but the amount of charge transfer must certainly decrease since pure Li is metallic. At such composi-

24

tions it will therefore be interesting to make a full analysis, including the possible existence of a polyhedral structure and the form of the high frequency longitudinal xx dispersion relation.

As a final comment, the fact that the minimum wavevector attainable in these simulations is not really very small leads to a situation where extrapolation of the dispersion relations towards $q = 0$ is not totally comfortable. The minimum wavevector is dictated by the size of the simulation sample, and decreasing q_{min} substantially requires an increase in the number of particles so high that it renders the FPMD simulations unfeasible. As an alternative, recently developed techniques, such as neural network potentials,[43,44] can be used to obtain the atomic forces and the energy in terms of the atomic positions in a fraction of the time needed for a DFT calculation. And if the neural networks are well trained with data provided by FPMD simulations then the accuracy of energies and forces will be at the same level as the DFT one. The good accuracy together with the fast computation will enable the simulation of much larger samples, thus allowing to reach smaller wavevectors, and increasing the confidence in the extrapolations towards zero. Moreover, simulations can be extended for a longer time so as to obtain better statistics for the properties studied. Also, it will turn feasible the study of the temperature and/or pressure variation of the properties of the systems, and include further atomic species in the simulations, which is at present prohibitively expensive using first principles calculations.

V. CONCLUSIONS

We have analyzed the behaviour of collective excitations corresponding to the mass-composition set of dynamic variables for three binary systems where the components have disparate masses.

We have observed a transition from mass-composition driven dynamics at small q to component-wise dynamics for larger wavevectors in the two systems where the heavy component is minoritary (UO_2 and Li_4Pb). This transition occurs at larger wavevectors for transverse dynamics than for longitudinal dynamics, and for systems with smaller mass ratio (UO_2) than for systems with a larger one (Li_4Pb). This transition is reflected in the dispersion relations through the appearance above the transition q-range of low frequency branches for the xx magnitudes in addition to the high frequency branches that exist at any q.

We have also observed that the high frequency longitudinal xx frequencies show in the case of Li_4Pb and UO_2 a strongly dispersive character that can be confused with the behaviour of an acoustic fast sound mode. However, taking into account also the transverse high frequency

dispersion branch, an extrapolation towards a finite non-zero frequency at $q = 0$ coincident with that of the transverse branch seems more physically appealing, and is consistent with the behaviour of optic excitations in non-ionic systems. Moreover, in the liquid LLE alloy there is no doubt that the high frequency *xx* branches are optic in character, since they are non-dispersive and tend to a common non-zero value at $q = 0$.

We have analyzed which characteristic features are common in the systems that appear to show fast sound and are absent in the LLE alloy, and can therefore be considered as candidates for enhancing the possible appearance of a dispersive longitudinal *xx* dispersion relation. We have identified both a common polyhedral structure and a common type of bonding characterized by some amount of charge transfer as opposed to a purely metallic bonding. Other common feature (apart from the large mass ratio between the components) is the fact that the heavy element is minoritary in molar terms. Additional studies for other systems are suggested in order to clarify the possible relationship between these characteristics and the appearance of fast sound.

Approaches alternative to FPMD, such as DFT-trained neural networks, are suggested as a means to explore smaller wavevectors and obtain clearer evidence of the nature of the high frequency longitudinal *xx* dispersion in systems where it is strongly dispersive, and additionally allow to study the temperature/pressure variation of the properties of the systems.

ACKNOWLEDGMENTS

DATA AVAILABILITY STATEMENT

The data that support the findings of this study are available from the corresponding author upon reasonable request.

REFERENCES

[1] Hohenberg P and Kohn W 1964 *Phys. Rev.* **136** B864; Kohn W and Sham L J 1965 *Phys. Rev.* **140** A1133

[2] Balucani U and Zoppi M 1994 *Dynamics of the Liquid State* (Clarendon, Oxford)

[3] Boon J P and Yip S 1980 *Molecular Hydrodynamics* (McGraw-Hill, New York)

[4] Hansen J P and McDonald I R 1986 *Theory of Simple Liquids* (Academic Press, New York)

[5] Montfrooij W and de Schepper I 2010 *Excitations in Simple Liquids, Liquid Metals and Superfluids* (Oxford University Press, Oxford)

[6] Bafile U, Guarini E and Barocchi F 2006 *Phys. Rev. E* **73** 061203

[7] Bryk T and Chushak Ya 1997 *J. Phys.: Condens. Matter* **9** 3329; Bryk T, Mryglod I and Kahl G 1997 *Phys. Rev. E* **56** 2903

[8] Bryk T, Mryglod I, Scopigno T, Ruocco G, Gorelli F and Santoro M 2010 *J. Chem. Phys.* **133** 024502

[9] Cunsolo A 2015 *Adv. Condens. Matter Phys.* **2015** 137435

[10] Cazzato S, Scopigno T, Bryk T, Mryglod I and Ruocco G 2008 *Phys. Rev. B* **77** 094204

[11] Bryk T, Kopcha M and Ruocco G 2023 *J. Mol. Liq.* **387** 122622

[12] Bosse J, Jacucci G, Ronchetti M and Schirmacher W 1986 *Phys. Rev. Lett.* **57** 3277

[13] de Jong P H K, Verkerk P, de Vroege C F, de Graaf L A, Howells W S and Bennington S M 1994 *J. Phys.: Condens. Matter* **6** L681

[14] Bryk T and Mryglod I 2004 *Cond. Matt. Phys.* **7** 285

[15] Bryk T and Wax J-F 2009 *Phys. Rev. B* **80** 184206

[16] Anento N, González L E, González D J, Chushak Y and Baumketner A 2004 *Phys. Rev. E* **70** 041201

[17] Campa A and Cohen E G D 1990 *Phys. Rev. A* **41** 5451

[18] Schram R P C, Wegdam G H and Bot A 1991 *Phys. Rev. A* **44** 8062

[19] Souto J, Alemany M M G, Gallego L J, González L E and González D J 2013 *Modelling Simul. Mater. Sci. Eng.* **21** 075006

[20] Nguyen V and Enderby J E 1977 *Phil. Mag.* **35** 1013

[21] Steinleitner G, Freyland W and Hensel F 1976 *Ber. Bunsenges. Phys. Chem.* **79** 1186

[22] Heitjans P, Kiese G, van der Marel C, Ackermann H, Bader B, Freiländer P and Stöckmann H J 1983 *Hyperfine Interact.* **15-16** 569

[23] Shimizu Y and Itami T 2004 *Mater. Transactions* **45** 2630

[24] Alemany M M G, Souto-Casares J, González L E and González D J 2021 *J. Mol. Liq.* **344** 117775

[25] Tsuji Y, Hashimoto W and Yoshizawa K 2019 *Bull. Chem. Soc. Jpn.* **92** 1154

[26] Price D L 2010 *High-temperature Levitated Materials* Cambridge University Press, Cambridge

[27] Guéneau C, Dupin N, Sundman B, Martial C, Dumas J-C, Gossé S, Chatain S, Bruycker F D, Manara D and Konings R J M 2011 *J. Nucl. Mater.* **419** 145

[28] Skinner L B, Benmore C J, Weber J K R, Williamson M A, Tamalonis A, Hebden A, Wiencek T, Alderman O L G, Guthrie M, Leibowitz L and Parise J B 2014 *Science* **346** 984

[29] Kronik L, Makmal A, Tiago M L, Alemany M M G, Jain M, Huang X Y, Saad Y and Chelikowsky J R 2006 *Phys. Status Solidi B* **243** 1063

[30] Kresse G and Hafner J 1993 *Phys. Rev.* B **47** 558; Kresse G and Hafner J 1994 *Phys. Rev.* B **49** 14251; Kresse G and Furthmuller J 1996 *Phys. Rev.* B **54** 11169; Kresse G and Furthmuller J 1996 *Comput. Mater. Sci.* **6** 15

[31] Blochl P E 1994 *Phys. Rev.* B **50** 17953; Kresse G and Joubert D 1999 *Phys. Rev.* B **59** 1758

[32] Chen J-L and Kaltsoyannis N 2022 *J. Phys. Chem. C* **126** 11426

[33] Ruppersberg H and Egger H 1975 *J. Chem. Phys.* **63** 4095; Ruppersberg H and Reiter H 1982 *J. Phys. F: Metal Phys.* **12** 1311

[34] Bryk T and Mryglod I 2004 *J. Phys.: Condens. Matter* **16** L463

[35] Gilbert E G, Johnson D W and Keerthi S S 1988 *IEEE Journal on Robotics and Automation*, **4** 193

[36] Stukowski A 2010 *Modelling Simul. Mater. Sci. Eng.* **18** 015012

[37] Waseda Y 1980 *The Structure of Non-Crystalline Materials*, McGraw-Hill, New York

[38] Cohen C, Sutherland J W H and Deutch, J M 1971 *Phys. Chem. Liq.* **2** 213

[39] Bhatia A B, Thornton D E and March N H 1974 *Phys. Chem. Liq.* **4** 97

[40] Slagle O D and Nelson R P 1971 *J. Nucl. Mater.* **40** 349

[41] Ruppersberg H and Speicher W 1976 *Z. Naturforsch. A* **31** 47; Saar J and Ruppersberg H 1987 *J. Phys. F: Metal Phys.* **17** 305

[42] Ueki Y, Hirabayashi M, Kunugi T, Yokomine T and Ara K 2009 *Fusion Sci. Technol.* **56** 846

[43] Behler J 2016 *J. Chem. Phys.* **145** 170901

[44] Deringer V L, Caro M A and Csányi G 2019 *Adv. Mater.* **31** 1902765